PAPER

Check for updates

One-step hydrothermal growth of porous nickel manganese layered double hydroxide nanosheet film towards efficient visible-light modulation†

Xingzhe Feng, Xinyi Wan, Ting Yang, Jiahui Huang, Jinmin Wang and Dongyun Ma *

Electrochromic smart windows have attracted great attention due to their dynamic regulation of the solar spectrum. NiO and MnO_2 are typical anodic coloration materials and widely investigated as complementary electrodes with WO_3. However, NiO and MnO_2 films often cannot be bleached to complete transparency, resulting in low transmittances and low optical modulations in the short-wavelength visible region. Herein, we report a porous nickel manganese layered double hydroxide (NiMn-LDH) nanosheet film directly grown on fluorine-doped tin oxide (FTO) glass using a one-step hydrothermal method, which demonstrates a high transmittance of 80.1% at 550 nm (without deduction of FTO glass). Induced by the double-redox couples of Ni^{2+}/Ni^{3+} and Mn^{3+}/Mn^{4+} associated synergistic electrochromic effect, the as-grown NiMn-LDH film electrode exhibits a large optical modulation of 68.5% at 550 nm, and a large solar irradiation modulation of 59.0% in the visible region of 400–800 nm. After annealing at 450 °C for 2 h, the NiMn-LDH film can be transformed into Ni_6MnO_8 film with a reduced optical modulation of 30.0% at 550 nm. Furthermore, the NiMn-LDH film electrode delivers an areal capacitance of 30.8 mF cm^{-2} at a current density of 0.1 mA cm^{-2}. These results suggest that the as-prepared NiMn-LDH film electrode is a promising candidate for both electrochromic and energy storage applications.

1 Introduction

Electrochromic (EC) devices have attracted great attention due to their dynamic regulation of the solar spectrum, and are promising for applications such as optical shutters, displays, optical filters, and smart windows.[1–3] Recently, energy-storage EC devices integrating EC and energy-storage functions in a single platform, such as EC batteries and EC supercapacitors, have developed rapidly for both energy-saving and energy-storage applications.[4–6] As the most important component, EC materials have been widely investigated as some of the promising smart materials, including transition metal oxides (WO_3,[7–9] V_2O_5,[10] NiO,[11] MoO_3,[12,13] *etc.*), conducting polymers,[14] small organic molecules,[15–17] Prussian blue (PB),[18–20] and so on.

Due to the advantages of high color contrast, good cycling stability, strong adhesion to conductive substrates and good thermal stability, transition metal oxides have been extensive studied for visible electrochromism. Among them, WO_3 was the earliest discovered cathodic coloration material, and can switch colors between colorless and blue states, resulting in a large optical modulation in the long-wavelength visible region.[21] In comparison, NiO and MnO_2, as typical anodic coloration materials, show reversible color change between light-yellow and brown states, and the optical modulation is mainly in short-wavelength visible region, which is the most comfortable neutral shade for human eyes and can be more easily recognized by the naked eye.[22] Hence, NiO or MnO_2 is often used as a counter electrode for WO_3 to construct complementary EC devices. However, NiO and MnO_2 films usually display a light-yellow color in the bleached state, and cannot be bleached to complete transparency, resulting in low transmittance and low optical modulation in the short-wavelength visible region. Therefore, it is imperative to seek new anodic coloration materials to achieve high transmittance (in their bleached states) and large optical modulations in the short-wavelength visible region, maximizing energy-saving.

Layered double hydroxides (LDHs) are favorable for redox reaction due to the special layered structure and abundant hydroxyl groups covalently bonded within interlayers, making them some of the most promising electrode materials for energy storage.[23–26] Guo *et al.*[27] have constructed hierarchical NiMn-LDH nanosheets on Ni foam by a one-step wet-chemical method, and the NiMn-LDH@Ni foam electrode was optimized by fine tuning the mole ratio of Ni to Mn, where a maximum specific capacitance of 1511 F g^{-1} was obtained at 2.5 A g^{-1}. Chen *et al.*[28] reported a hierarchical 3D carbon-coated NiMn-LDH grown on Ni foam through a two-step hydrothermal

School of Materials and Chemistry, University of Shanghai for Science and Technology, Shanghai 200093, China. E-mail: dyma@usst.edu.cn

† Electronic supplementary information (ESI) available. See DOI: https://doi.org/10.1039/d4ra00209a

method. The resulting composite displayed a high specific capacitance of 1916 F g^{-1} at 0.5 A g^{-1} and an excellent cycling stability. The above results indicate that NiMn-LDH is a superb candidate for energy storage. In addition to the applications in supercapacitors,[29] LDHs have many other applications such as water splitting, carbon dioxide reduction, and batteries/full cells.[30,31] In recent years, some LDHs were investigated for EC applications, such as ZnO@Ni/Co-LDH[32] and PEDOT:PSS/LDH.[33] However, their optical modulation is often lower than 60%. Moreover, NiMn-LDH has rarely been reported for EC applications.

Herein, we demonstrate a porous NiMn-LDH nanosheets film for visible electrochromism, which can be directly grown on fluorine-doped tin oxide (FTO) glass by a one-step hydrothermal process. The as-grown NiMn-LDH film exhibits a high transmittance of 80.1% at 550 nm (without deduction of FTO glass). Compared to single NiO or MnO$_2$, the reversible double-redox couples of Ni^{2+}/Ni^{3+} and Mn^{3+}/Mn^{4+} enable a synergistic EC effect, and thus a large optical modulation of 68.5% at 550 nm is achieved for the NiMn-LDH film electrode. Furthermore, the obtained NiMn-LDH film electrode delivers an areal capacitance of 30.8 mF cm^{-2} at a current density of 0.1 mA cm^{-2}. Although our results confirm that NiMn-LDH is promising for both energy-saving and energy-storage applications, there is still room for improvement in the cycling stability of the NiMn-LDH film electrode.

2 Experimental section

2.1 Materials

Materials and reagents used for the preparation of NiMn-LDH film including Nickel chloride hexahydrate (NiCl$_2$·6H$_2$O, 99%), manganese(II) sulfate monohydrate (MnSO$_4$·H$_2$O, 99%), Urea (NH$_2$CONH$_2$, 99%), ammonium fluoride (NH$_4$F, 98%). All chemicals were used without further modifications.

2.2 Preparation of precursor solution

All chemicals were purchased from Shanghai Titan Scientific Co. Ltd, and used without further purification. The NiMn-LDH film was successfully grown on fluorine-doped tin oxide (FTO) transparent conductive glasses through a one-step hydrothermal method. The precursor solution for hydrothermal use was made by dissolving 0.04 g MnSO$_4$, 0.18 g NiCl$_2$·6H$_2$O, 0.19 g NH$_4$F and 0.20 g urea in 50 mL of deionized water under magnetic stirring at room temperature.

2.3 Growth of NiMn-LDH and Ni$_6$MnO$_8$ films

FTO glasses purchased from Zhuhai Kaivo Optoelectronic Technology Co., Ltd (China) were used as the substrates, which were first ultrasonically cleaned with deionized water and ethanol in turn, and then dried in an oven before use. For growth of NiMn-LDH film, 32 mL of the above precursor solution was transferred into a Teflon-lined stainless-steel autoclave. A piece of cleaned FTO glass with one end wrapped with polytetrafluoroethylene tape was placed into the autoclave and leaned on the wall with the conductive side facing down.[34] The

autoclave was subsequently sealed and maintained at 160 °C for 4 h. After cooling to room temperature, the NiMn-LDH film coated FTO glass was taken out, rinsed with deionized water and dried naturally. Finally, the as-grown NiMn-LDH films were annealed at 450 °C for 2 h, and then Ni$_6$MnO$_8$ films were obtained. The hydrothermal growth process of the NiMn-LDH film and subsequent annealing process is summarized in Fig. S1.†

2.4 Material characterization

The morphology, structure, and chemical composition of the as-prepared NiMn-LDH films were investigated using X-ray diffraction (XRD, D8 ADVANCE, Bruker, Germany) with a step size of 6° min^{-1} over the 2θ range of 10–80°, scanning electron microscopy (SEM, JEOL, JSM-IT500HR, Hitachi, Japan) operated at 20 kV and 40 mA, laser confocal micro-Raman spectroscopy (Raman, LabRAM HR Evolution, HORIBA Scientific, Japan) using a 532 nm laser excitation with a resolution of 1 cm^{-1} and X-ray photoelectron spectrometry (XPS, ESCA-LAB 250Xi, Thermo Fisher Scientific, USA). The XPS data was analysed by a software of Avantage. The thermal stabilization of the as-prepared NiMn-LDH films was characterized using a thermal analyzer (TG/DTA, 7300, Hitachi, Japan) from room temperature to 800 °C at a heating rate of 10 °C min^{-1}, where the NiMn-LDH powders were scraped from the FTO glasses.

2.5 Electrochemical and electrochromic performances

Electrochemical measurements such as cyclic voltammetry (CV) curves, electrochemical impedance spectroscopy (EIS), charging/discharging curves at different current densities were recorded by an electrochemical workstation (CHI760E, Shanghai Chenhua Instruments Co., Ltd, China) in a three-electrode system, which consisted of the NiMn-LDH working electrode, a Pt sheet counter electrode and Hg/HgO reference electrode. 1 mol L^{-1} of KOH aqueous solution was used as electrolyte. Spectroscopy testing was conducted using a UV/visible/near infrared (NIR) spectrometer (UV5700, Hitachi, Japan) in the range of 400–800 nm with a resolution of 1 nm. The in situ transmittance spectra of the films before and after switching were recorded over a wavelength range from 400 to 800 nm. The switching responses of the NiMn-LDH film were measured at 550 nm. The switching times (coloration time t_c and bleaching time t_b) are defined as the times required for 90% of change in the full optical modulation at the specified wavelength.

3 Results and discussion

3.1 Structural and morphological characterization

The NiMn-LDH film was grown directly on FTO glass using a one-step hydrothermal method, and the crystalline phase was examined by XRD, as depicted in Fig. 1a. Excluding the diffraction peaks of bare FTO glass (JCPDS no. 41-1445), the diffraction peaks of the hydrothermally grown NiMn-LDH film can be ascribed to (006), (012), (110) and (113) planes of NiMn-LDH, which is consistent with those of the previous literature.[35,36] This indicates that the NiMn-LDH film is successfully
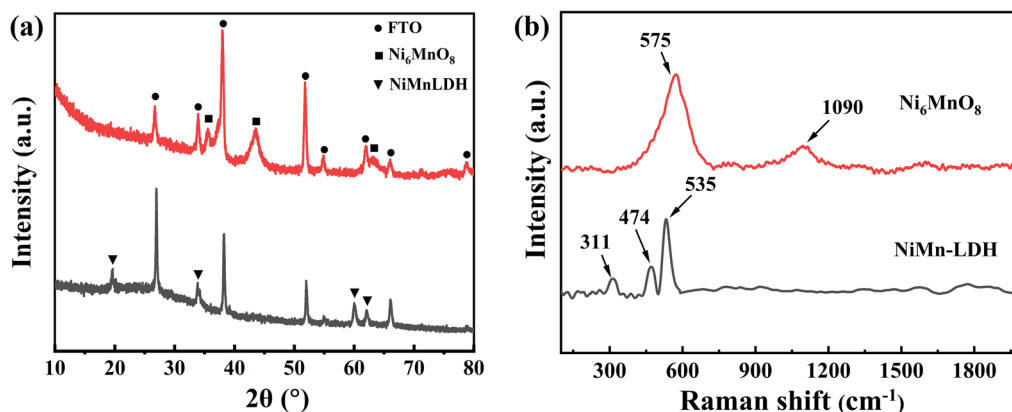
Fig. 1 Structure characterization. (a) XRD patterns of the as-grown NiMn-LDH film (black line) and the film annealed at 450 °C (red line). (b) Raman spectra of NiMn-LDH and Ni_6MnO_8 films.

coated onto FTO glass. Raman spectrum of the NiMn-LDH film is presented in Fig. 1b, where the peaks centered at 311, 474, 535 cm^{-1} (M–O–M bond) further validate the effective synthesis of NiMn-LDH.[37–39] The thermal stability of the NiMn-LDH film was characterized by thermogravimetric (TG) analyzer, and the result is shown in Fig. S2.† According to the TG curve, the weight loss from room temperature to 450 °C is approximately 15%, which mainly due to the removal of adsorbed water and crystalline water from NiMn-LDH. The main characteristic peaks at $2\theta = 35.8$, 43.5 and 63.3° observed in the XRD pattern (Fig. 1a) of the film annealed at 450 °C correspond to cubic Ni_6MnO_8 phase (JCPDS no. 42-0479).[40] The Raman peaks located at 575 and 1090 cm^{-1} (Fig. 1b) are consistent with the Raman diffraction peaks of Ni_6MnO_8 reported in the previous literature.[41,42] Therefore, the hydrothermally grown NiMn-LDH film can be transformed into Ni_6MnO_8 after annealing at 450 °C for 2 h.

According to the previous literatures,[43–45] various microstructural parameters were calculated from the XRD data and 2θ values of the diffraction peaks, as described in ESI.† The calculated results (Table S1†) show that the average crystallite size (D) of the NiMn-LDH (22.6 nm) is bigger than that of Ni_6MnO_8 (9.9 nm). While Ni_6MnO_8 exhibit larger lattice strain (ε) and dislocation density (δ) than those of NiMn-LDH. The bigger value of D and smaller ε and δ indicate a higher crystallinity of NiMn-LDH, which also can be observed from the diffraction peaks in Fig. 1a.

XPS was employed to analyze the chemical compositions and valence states of elements in the bleached and colored NiMn-LDH films. The survey spectrum confirms the existence of Ni, Mn, and O elements in the bleached NiMn-LDH film (Fig. S3†). The peaks at 855.3 and 873.1 eV, depicted in the XPS spectrum of Ni 2p (Fig. 2a), correspond to the binding energies of Ni^{2+} $2p_{3/2}$ and $2p_{1/2}$ species, which reveals that the valence state of Ni in the bleached NiMn-LDH film is +2. As observed from XPS spectrum of Mn 2p (Fig. 2b), the Mn $2p_{3/2}$ peak can be deconvoluted into three subpeaks at 637.2, 642.0 and 646.8 eV, which indicate the presence of Mn^{2+}, Mn^{3+} and Mn^{4+}, respectively.[46] The peak at 653.3 eV is attributed to Mn $2p_{1/2}$. Fig. 2c reveals the

fitted O 1s spectrum, where two peaks at 530.6 and 531.2 eV can be attributed to M–O–M and M–O–H (M: Ni or Mn) bonds, and the peak at 532.2 eV is derived from H–O–H bond, which further demonstrates the formation of NiMn-LDH.[47] We further investigated the XPS spectra of the NiMn-LDH film in its coloration state. Fig. 2d presents XPS spectrum of Ni 2p, where the relative content of Ni^{3+} is increased, indicating that Ni^{2+} is partially oxidized to Ni^{3+} during the coloration process. The ratio of Mn^{4+} to Mn^{3+} is simultaneously increased (Fig. 2e), which indicates that partial Mn^{3+} ions are also oxidized to Mn^{4+} ions. As observed in Fig. 2f, the M–O–H/M–O–M ratio is also dramatically increased, which is attributed to the intercalation of OH$^-$ ions during the coloration process. The above results confirm that the reversible redox reactions of Ni^{2+}/Ni^{3+} and Mn^{3+}/Mn^{4+} during the bleaching/coloration process are associated with the intercalation and deintercalation of OH$^-$ ions.

SEM images, depicted in Fig. 3a and b, reveal that the FTO glass is uniformly coated by the NiMn-LDH film with a thickness of about 654 nm after hydrothermal growth. The as-prepared NiMn-LDH film is composed of extremely thin nanosheets (~26.2 nm), forming a porous surface. Moreover, the NiMn-LDH nanosheets are almost perpendicular to the FTO glass (inset of Fig. 3b). This porous structure not only provides good contact between electrolyte solution and the NiMn-LDH films, but also provides large channels for the intercalation/deintercalation of OH$^-$ ions.[48,49] The formation mechanism of NiMn-LDH nanosheets is similar to that of the previous reported NiCo-LDH nanosheets.[50] Firstly, Ni^{2+} and Mn^{2+} reacted with OH$^-$ to form Ni and Mn hydroxide monomers during the hydrothermal condition, which precipitated as nuclei and quickly grew into host nanoparticles. Then, these primary particles aggregated into chains and deposited on the FTO substrate, forming the aggregation cores. As the primary particles continued to aggregate through olation reactions with each other, they began to crystallize and grow along the c-axis with the assistance of NH$_4$F, and finally forming the NiMn-LDH nanosheets. The uniform distributions of Mn, Ni and O are observed in the corresponding elemental distribution mapping (Fig. 3c), which further confirms the successful formation of
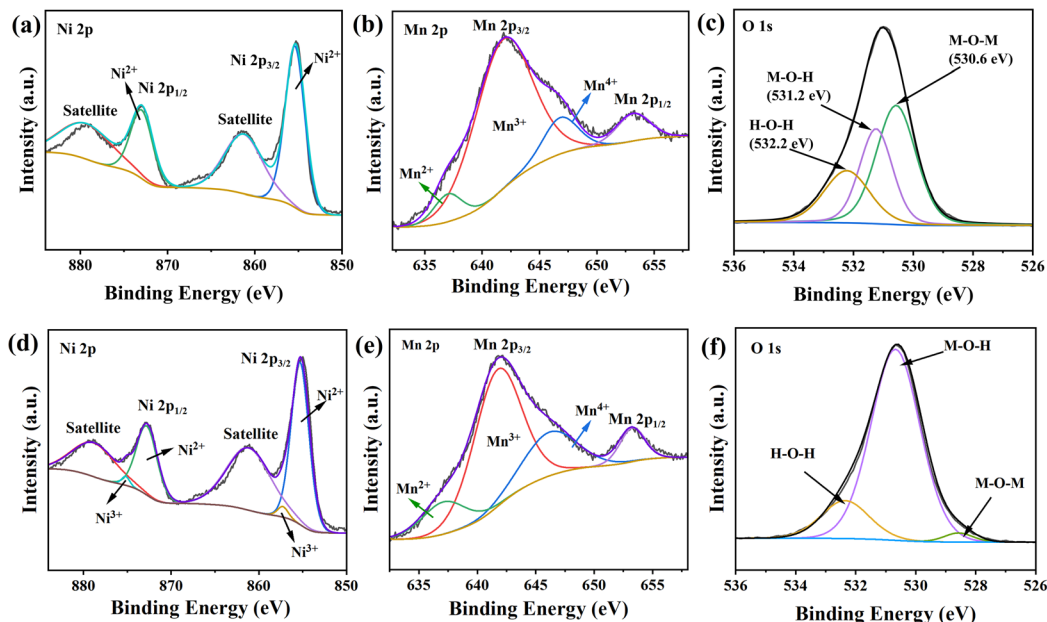
Fig. 2 Chemical composition. XPS spectra of (a) Ni 2p, (b) Mn 2p and (c) O 1s for the bleached NiMn–LDH film. XPS spectra of (d) Ni 2p, (e) Mn 2p and (f) O 1s for the colored NiMn–LDH film.
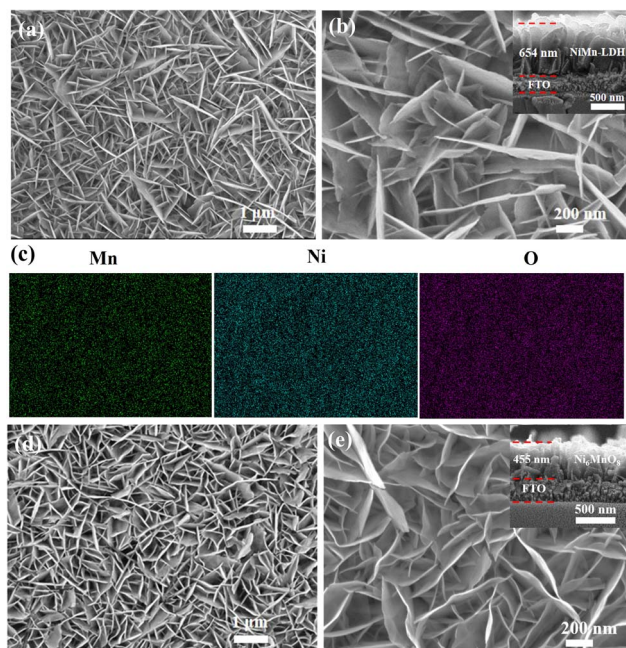

Fig. 3 Morphology characterization. (a and b) SEM images and (c) corresponding EDS elemental mapping of the NiMn–LDH film. (d and e) SEM images of the annealed Ni_6MnO_8 film. Insets of (b) and (e) are the cross-sectional views of the NiMn–LDH and Ni_6MnO_8 films, respectively.

pure NiMn-LDH film. After annealing at 450 °C, the morphology of the Ni_6MnO_8 film remains almost unchanged (Fig. 3d and e), while the thicknesses of the film and nanosheets are decreased to 455 nm and 15.8 nm, respectively. The decrease in thickness may be related to the removal of adsorbed water and crystalline

water occurred conjointly with the dehydroxylation of NiMn-LDH during the annealing process.

3.2 Electrochromic and electrochemical performances

Fig. 4a presents the colors of the NiMn-LDH film in its colored and bleached states. The as-grown NiMn-LDH film displays a reversible color change between almost colorless (bleached at −1.2 V) and brownish-black (colored at 1.0 V) states. This neutral color is more comfortable to human eyes, and can be more easily recognized by our naked eyes. Furthermore, the NiMn-LDH film (with deduction of FTO glass) exhibits a high transmittance of 92.0% at 550 nm (Fig. 4b), while a high transmittance of 80.1% is also achieved for the NiMn-LDH electrode (without deduction of FTO glass). Thus, the NiMn-LDH film electrode shows a high optical modulation of 68.5% at 550 nm (Fig. 4c), which is much larger than those of the previously reported NiO (46.0%),[51] MnO_2 (42.3%)[52] and PEDOT:PSS/LDH (32.0%)[33] films. In comparison, the annealed Ni_6MnO_8 film electrode cannot be bleached to complete transparency, resulting in a low transmittance in the bleached state. Therefore, a much lower optical modulation of 30.0% at 550 nm is obtained for the Ni_6MnO_8 film electrode. For evaluation of the actual solar irradiation modulation, the solar irradiance transmittance of the NiMn-LDH and Ni_6MnO_8 film electrodes in different states are calculated and presented in Fig. 4d and e. The calculations are based on the following formula:[53]

$$T' = \int \varphi(\lambda) T(\lambda) \mathrm{d}\lambda / \int \varphi(\lambda) \mathrm{d}\lambda \qquad (1)$$

where $T(\lambda)$ is the transmittance at a wavelength of λ and $\varphi(\lambda)$ is the solar irradiance at 1.5 air mass. The colored NiMn-LDH film electrode could effectively block 87.3% of solar irradiance in the visible region of 400–800 nm, which is much higher than that of
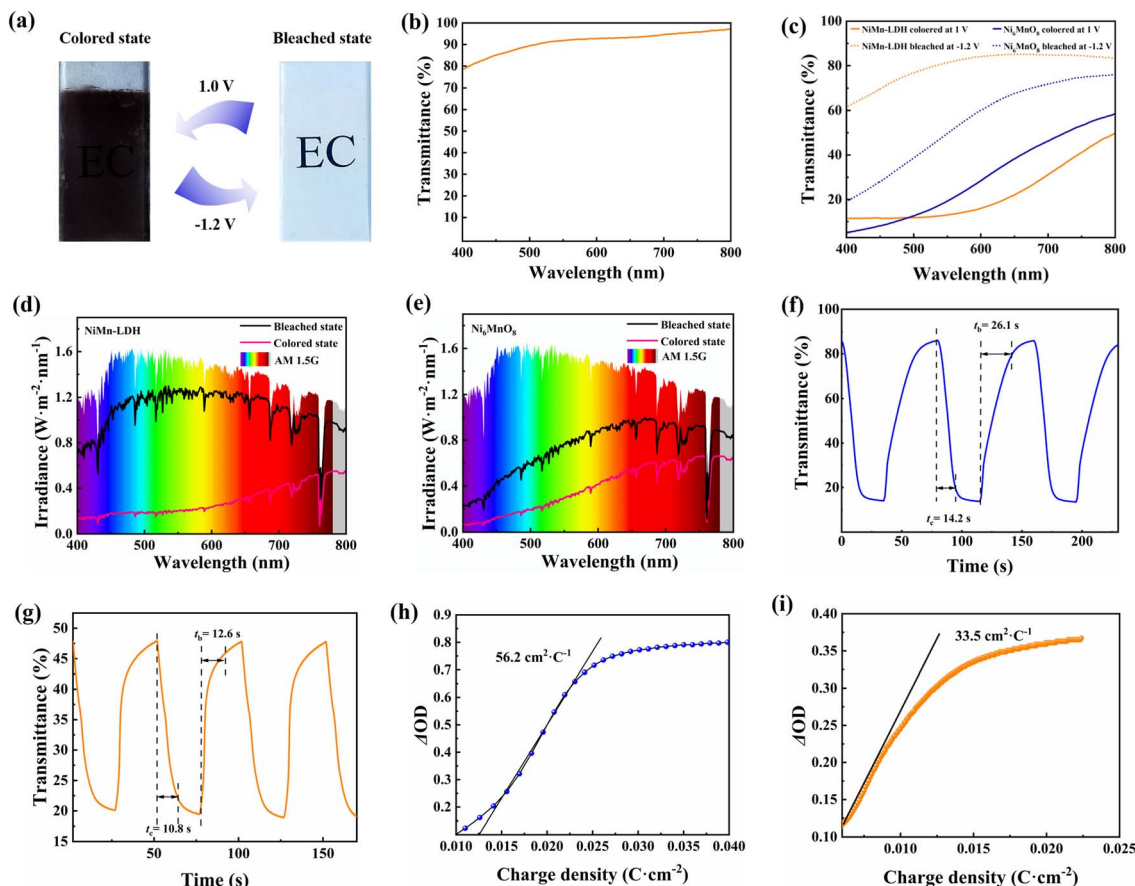
Fig. 4 Electrochromic performance. (a) Digital photos of the NiMn-LDH film electrode in the colored and bleached states. (b) Transmittance spectrum of the as-grown NiMn-LDH film with deduction of FTO glass. (c) Transmittance spectra of the NiMn-LDH and Ni_6MnO_8 film electrodes in their colored and bleached states. Solar irradiance spectra of (d) the NiMn-LDH and (e) Ni_6MnO_8 film electrodes. Real-time transmittance changes of (f) the NiMn-LDH and (g) Ni_6MnO_8 film electrodes recorded at 550 nm. Optical density variation with respect to the charge density of (h) the NiMn-LDH and (i) Ni_6MnO_8 film electrodes measured at 550 nm.

the Ni_6MnO_8 film electrode (68.7%). Therefore, the NiMn-LDH film electrode exhibits a larger solar irradiation modulation (59.0%) than the Ni_6MnO_8 film electrode (25.5%) in the visible region of 400–800 nm.

The response times of the NiMn-LDH and Ni_6MnO_8 films are calculated from real-time transmittance spectra measured under periodic potentials of 1.0 V (coloration) and −1.2 V (bleaching). The corresponding time–current curves of the two film electrodes are recorded in Fig. S4 and S5.† The response times of the NiMn-LDH film electrode are calculated to be 14.2 s for coloration and 26.1 s for bleaching (Fig. 4f), which are faster than those of the reported pure NiO film electrode (9.0 s for coloration and 38.9 s for bleaching).[54] The response time is related to many factors, such as the test conditions, the size and thickness of the film, microstructure and intrinsic property of the EC materials.[42] Due to the thinner thickness and lower optical modulation, shorter response times (10.8 s for coloration and 12.6 s for bleaching, respectively) are achieved for the Ni_6MnO_8 film electrode (Fig. 4g). Coloration efficiency (CE) is one of the most important parameters for evaluating the EC performance, which can be calculated from the following formulae:[29]

$$CE = \Delta OD/(Q/A) \quad (2)$$

$$\Delta OD = \log(T_b/T_c) \quad (3)$$

where Q/A is the injected charge Q per unit electrode area A. T_b and T_c are the transmittances in the bleached and colored states at 550 nm, respectively. A calculated CE value of 56.2 cm^2 C^{-1} is obtained for the NiMn-LDH film electrode (Fig. 4h), which is higher than 33.5 cm^2 C^{-1} of the Ni_6MnO_8 film electrode (Fig. 4i) and those of the single NiO (16.95 cm^2 C^{-1})[53] and MnO_2 (28 cm^2 C^{-1})[55] films. By applying periodic potentials of 1.0 V for 35 s and −1.2 V for 45 s, the optical modulation of the NiMn-LDH film electrode still maintains 79.8% of its initial value after 8000 s (Fig. S6†). While the Ni_6MnO_8 film electrode exhibits a better cycle stability, retaining 95.3% of its optical modulation after 16 000 s (Fig. S7†). This may due to the structural stability, the smaller optical modulation of the Ni_6MnO_8 film and better adhesion between the Ni_6MnO_8 film and FTO glass. Additionally, several key EC performances are summarized in Table S2† to compare the present work with some other LDHs films. The results indicate that our NiMn-LDH film provides larger optical
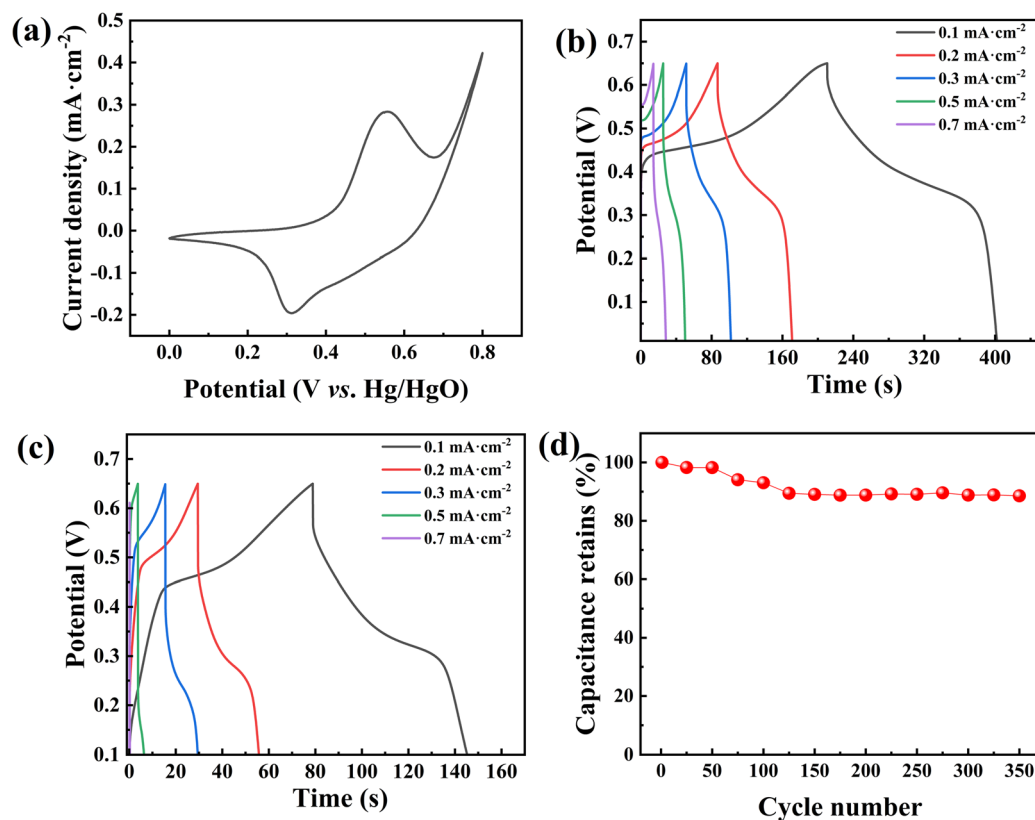
Fig. 5 Electrochemical performance. (a) CV curve of the NiMn–LDH film electrode scanned at 5 mV s^{-1}. GCD curves for (b) NiMn–LDH and (c) Ni$_6$MnO$_8$ film electrodes measured at different current densities. (d) Cycling performance of the NiMn–LDH film electrode at a current density of 0.1 mA cm^{-2}.

modulation than the ZnO@Ni/Co-LDH and PEDOT:PSS/LDH films, faster switching times than NiAl-LDH film.

The electrochemical performance of the as-prepared film electrodes was investigated by cyclic voltammetry (CV) and galvanostatic charging/discharging (GCD) in 1.0 mol L^{-1} KOH solution. Fig. 5a shows the CV curve of NiMn–LDH film electrode in a potential range of 0–0.8 V at a scan rate of 50 mV s^{-1}, where a couple of wide oxidation and reduction peaks is observed. The distinct redox peaks indicate a typical pseudocapacitive behaviour due to the reversible Faraday redox reaction.[24,30] According to the XPS results, the reversible redox process is originated from the reversible redox reactions between Ni^{2+}/Ni^{3+} and Mn^{3+}/Mn^{4+}, and accompanied by the intercalation and deintercalation of OH$^-$ ions.[43] Additionally, the current response increases accordingly with the increasing scan rates for both the NiMn–LDH (Fig. S8†) and Ni$_6$MnO$_8$ (Fig. S9†) film electrodes, indicating good rate capability.[24,56]

Fig. 5b and c present GCD curves of the NiMn–LDH and Ni$_6$MnO$_8$ film electrodes at different current densities. The discharge specific capacitance can be calculated by the following formula:[57]

$$C_s = I\Delta t / S\Delta V \qquad (4)$$

where C_s denotes the specific capacitance, I and S are the discharge current and the area of the as-prepared film, respectively. Δt and ΔV denote the discharge time and the working

potential window, respectively. As shown in Fig. 5b and c, the charging and discharging processes of the NiMn–LDH and Ni$_6$MnO$_8$ film electrodes will take longer time upon reducing the current density, implying a typical redox pseudocapacitance mechanism.[46] Therefore, the NiMn–LDH film electrode delivers a high specific capacitance value of 30.8 mF cm^{-2} at a current density of 0.1 mA cm^{-2}, which is much higher than that of the Ni$_6$MnO$_8$ film electrode (10.2 mF cm^{-2} at 0.1 mA cm^{-2}). The better capacitive behavior of the NiMn–LDH film electrode might be related to its lower resistance and better electric conductivity, which is estimated by electrochemical impedance spectroscopy (Fig. S10†), where the NiMn–LDH film electrode demonstrates a smaller charge transfer resistance (19.8 Ω) than the Ni$_6$MnO$_8$ film electrode (49.1 Ω). The specific capacitance value of the NiMn–LDH film electrode is also higher than those of other LDHs, such as ZnO@Ni/Co-LDH (49.7 mC cm^{-2}),[32] NiMn-LDHs (3.0 mF cm^{-2}) and NiCoLDHs (4.9 mF cm^{-2}).[58] Furthermore, the NiMn–LDH film electrode exhibits a good charge/discharge cycling stability at 0.1 mA cm^{-2}, maintaining 90% of the specific capacitance after 350 cycles (Fig. 5d).

4 Conclusions

In summary, we have successfully demonstrated a porous NiMn-LDH film hydrothermally grown on FTO glass for visible electrochromism and energy-storage applications. The obtained

film is composed of extremely thin NiMn-LDH nanosheets, which are almost perpendicular to the FTO glass. After annealing at 450 °C for 2 h, the NiMn-LDH film can be transformed into Ni_6MnO_8 film. In comparison, the porous NiMn-LDH film electrode can be bleached to almost colorless, resulting in a high transmittance of 80.1% at 550 nm. Furthermore, the double redox couples of Ni^{2+}/Ni^{3+} and Mn^{3+}/Mn^{4+} enable the NiMn-LDH film electrode a large optical modulation of 68.5% at 550 nm, and a large solar irradiation modulation of 59.0% in the visible region of 400–800 nm. The NiMn-LDH film electrode also delivers an areal capacitance of 30.8 mF cm^{-2} at a current density of 0.1 mA cm^{-2}. The good EC and electrochemical performances of the NiMn-LDH film electrode provide a new strategy for developing high-performance EC devices based on layered double hydroxide.

Author contributions

Xinzhe Feng: data curation, methodology, formal analysis, investigation, writing – original draft. Xinyi Wan: data curation. Ting Yang: data curation. Jiahui Huang: data curation. Jinmin Wang: conceptualization, funding acquisition, writing – review & editing. Dongyun Ma: conceptualization, supervision, funding acquisition, writing – review & editing.

Conflicts of interest

There are no conflicts to declare.

Acknowledgements

Notes and references

1 H. Li and A. Y. Elezzabi, *Nanoscale Horiz.*, 2020, **5**, 691–695.
2 S. J. Lee, D. S. Choi, S. H. Kang, W. S. Yang, S. Nahm, S. H. Han and T. Kim, *ACS Sustain. Chem. Eng.*, 2019, **7**, 7111–7117.
3 L. Wang, X. Jiao, D. Chen and T. Wang, *Adv. Sci.*, 2021, **9**, 2104121.
4 J. Wang, L. Zhang, L. Yu, Z. Jiao, H. Xie, X. W. Lou and X. W. Sun, *Nat. Commun.*, 2014, **5**, 4921.
5 G. Cai, R. Zhu, S. Liu, J. Wang, C. Wei, K. J. Griffith, Y. Jia and P. S. Lee, *Adv. Energy Mater.*, 2022, **12**, 2103106.
6 F. Zhao, B. Wang, W. Zhang, S. Cao, L. Liu, A. Y. Elezzabi, H. Li and W. W. Yu, *Mater. Today*, 2023, **66**, 431–447.
7 Y. Huang, B. Wang, P. Lyn, S. Zhao, X. Wu, S. Zhang, R. Li, Q. Jiang, F. Wang, Y. Zhao and R. Zhang, *Nano Res.*, 2023, **16**, 12165–12172.
8 B. Faceira, L. Teule-Gay, G. M. Rignanese and A. Rougier, *J. Phys. Chem.*, 2019, **201**, 110114.
9 J. Guo, H. Jia, Z. Shao, P. Jin and X. Cao, *Acc. Mater. Res.*, 2023, **4**, 438–447.
10 I. Mjejri, M. Duttine, S. Buffiere, C. Labrugere-Sarroste and A. Rougier, *Inorg. Chem.*, 2022, **61**, 18496–18503.
11 G. Cai, X. Wang, M. Cui, P. Darmawan, J. Wang, A. L.-S. Eh and P. S. Lee, *Nano Energy*, 2015, **12**, 258–267.
12 Y. Kim, J. H. Lee, Y. H. Jung, D. Lee and J. Son, *Mater. Horiz.*, 2022, **9**, 1631–1640.
13 B. Ezhilmaran and S. V. Bhat, *Chem. Eng. J.*, 2022, **446**, 136924.
14 M. Han, C. H. Cho, H. Jang and E. Kim, *J. Mater. Chem. A*, 2021, **9**, 16016–16027.
15 G. K. Pande, J. S. Heo, J. H. Choi, Y. S. Eom, J. Kim, S. K. Park and J. S. Park, *Chem. Eng. J.*, 2021, **420**, 130446.
16 A. N. Woodward, J. M. Kolesar, S. R. Hall, N.-A. Saleh, D. S. Jones and M. G. Walter, *J. Am. Chem. Soc.*, 2017, **139**, 8467–8473.
17 Z. Wang, X. Jia, P. Zhang, Y. Liu, H. Qi, P. Zhang, U. Kaiser, S. Reineke, R. Dong and X. Feng, *Adv. Mater.*, 2021, **34**, 2106073.
18 J. Qian, D. Ma, Z. Xu, D. Li and J. Wang, *Sol. Energy Mater. Sol. Cells*, 2018, **177**, 9–14.
19 Y. Ding, H. Sun, Z. Li, C. Jia, X. Ding, C. Li, J.-G. Wang and Z. Li, *J. Mater. Chem. A*, 2023, **11**, 2868–2875.
20 B. Huang, J. Song, J. Zhong, H. Wang, X. Zheng, J. Jia, S. Yun, D. You, H. Kimura and L. Kang, *Chem. Eng. J.*, 2022, **449**, 137850.
21 S. K. Deb, *Appl. Opt.*, 1969, **8**, 192–195.
22 C. G. Granqvist, *Adv. Mater.*, 2003, **15**, 1789–1803.
23 J. Hu, X. Tang, Q. Dai, Z. Liu, H. Zhang, A. Zheng, Z. Yuan and X. Li, *Nat. Commun.*, 2021, **12**, 3409.
24 Z. Hou, J. Yu, X. Zhou, Z. Chen, J. Xu, B. Zhao, W. Gen and H. Zhang, *J. Colloid Interface Sci.*, 2023, **646**, 753–762.
25 F. Zhu, L. Sun, Y. Liu and W. Shi, *J. Mater. Chem. A*, 2022, **10**, 21021–21030.
26 Y. Wang, C. Xiang, Z. Xiao, F. Xu, L. Sun, J. Zhang and Y. Zou, *J. Energy Storage*, 2021, **44**, 103311.
27 X. Guo, X. Liu, X. Hao, S. Zhu, F. Dong, Z. Wen and Y. Zhang, *Electrochim. Acta*, 2016, **194**, 179–186.
28 H. Chen, Y. Ai, F. Liu, X. Chang, Y. Xue, Q. Huang, C. Wang, H. Lin and S. Han, *Electrochim. Acta*, 2016, **213**, 55–65.
29 H. Wang, H. Zeng, K. Zhang, S. Lv, W. Yan, Z. Tang and C. Luo, *J. Alloys Compd.*, 2024, **972**, 172701.
30 Q. Shi, M. Cheng, Y. Liu, J. Wang, G. Zhang, L. Li, L. Du, G. Wang and H. Liu, *Coord. Chem. Rev.*, 2024, **499**, 215500.
31 G. Sriram, S. Thangarasu, K. Selvakumar, M. Kurkuri, N. R. Dhineshbabu and T. H. Oh, *Colloids Surf., A*, 2024, **685**, 133199.
32 X. Liu, J. Wang, D. Tang, Z. Tong, H. Ji and H. Qu, *J. Mater. Chem. A*, 2022, **10**, 12643–12655.
33 A. Zhou, X. Liu, Y. Dou, S. Guan, J. Han and M. Wei, *J. Mater. Chem. C*, 2016, **4**, 8284–8290.
34 J. Sun, X. Wan, T. Yang, D. Ma and J. Wang, *Sol. Energy Mater. Sol. Cells*, 2023, **256**, 112318.
35 Y. Tang, H. Shen, J. Cheng, Z. Liang, C. Qu, H. Tabassum and R. Zou, *Adv. Funct. Mater.*, 2020, **30**, 1908223.

36 Y. Li, J. Shi, L. Wu, J. Zhang and J. Lu, *Eur. J. Inorg. Chem.*, 2021, **2021**, 620–627.

37 M. M. Baig, I. H. Gul, R. Ahmad, S. M. Baig, M. Z. Khan and N. Iqbal, *J. Mater. Sci.*, 2021, **56**, 18636–18649.

38 X. Yang, H. Zhang, W. Xu, B. Yu, Y. Liu and Z. Wu, *Catal. Sci. Technol.*, 2022, **12**, 4471–4485.

39 A. Emin, J. Li, Y. Dong, Y. Fu, D. He and Y. Li, *J. Energy Storage*, 2023, **65**, 107340.

40 S. E. S. Monica, C. R. Dhas, R. Venkatesh, R. Sivakumar, R. Vignesh and V. A. Ferby, *J. Solid State Electrochem.*, 2022, **26**, 1271–1290.

41 T. Li, K. Chang, A. M. Hashem, A. E. Abdel-Ghany, R. S. El-Tawil, H. Wang, H. El-Mounayri, A. Tovar, L. Zhu and C. M. Julien, *Electrochem*, 2021, **2**, 95–117.

42 J. Zhang, R. Hu, P. Dai, Z. Bai, X. Yu, M. Wu and G. Li, *J. Mater. Sci.: Mater. Electron.*, 2018, **29**, 7510–7518.

43 S. Supriya, S. Das, S. Senapati and R. Naik, *J. Am. Ceram. Soc.*, 2023, **106**, 5955–5964.

44 P. Priyadarshini, S. Das, D. Alagarasan, R. Ganesan, S. Varadharajaperumal and R. Naik, *Sci. Rep.*, 2021, **11**, 21518.

45 A. Parida, S. Senapati, S. Samal, S. Bisoyi and R. Naik, *ACS Appl. Nano Mater.*, 2023, **6**, 11230–11241.

46 F. Lu, Y. Ji, D. Shi, J. Yao and L. Pei, *J. Colloid Interface Sci.*, 2023, **641**, 510–520.

47 J.-Q. Xie, L. Jiang, J. Chen, D. Mao, Y. Ji, X.-Z. Fu, R. Sun and C.-P. Wong, *Chem. Eng. J.*, 2020, **393**, 124598.

48 H. Fu, A. Zhang, H. Zong, F. Jin, H. Guo and J. Liu, *J. Colloid Interface Sci.*, 2023, **629**, 938–949.

49 S. Wang, X. Duan, T. Gao, Z. Wang, D. Zhou, K. Sun, Z. Shang, Y. Kuang, S. Tian, X. Li, W. Liu and X. Sun, *J. Electrochem. Soc.*, 2020, **167**, 160550.

50 H. Chen, L. Hu, M. Chen, Y. Yan and L. Wu, *Adv. Funct. Mater.*, 2014, **24**, 934–942.

51 K. Xu, L. Wang, G. Liu, C. Ge, L. Wang, W. Wang and M. Chen, *Energy Environ. Mater.*, 2022, **6**, 12362.

52 L. Zhao, Z. Chen, Y. Peng, L. Yang, J. Ai, J. Zhou and L. Miao, *Sustainable Mater. Technol.*, 2022, **32**, 00445.

53 D. Ma, A. Lee-Sie Eh, S. Cao, P. S. Lee and J. Wang, *ACS Appl. Mater. Interfaces*, 2022, **14**, 1443–1451.

54 H. S. Chavan, B. Hou, Y. Jo, A. I. Inamdar, H. Im and H. Kim, *ACS Appl. Mater. Interfaces*, 2021, **13**, 57403–57410.

55 D. Zhou, B. Che and X. Lu, *J. Mater. Chem. C*, 2017, **5**, 1758–1766.

56 Y. Chen, J. Sun, Y. Huang, D. Lin, D. Ma and J. Wang, *Ceram. Int.*, 2023, **49**, 29534–29541.

57 N. S. Tantawy, F. El-Taib Heakal and S. Y. Ahmed, *J. Energy Storage*, 2020, **31**, 101625.

58 B. Liu, M. Zhang, Y. Wang, Z. Chen and K. Yan, *J. Alloys Compd.*, 2021, **852**, 156949.